Titanium porous-transport layers for PEM water electrolysis prepared by tape casting

Jason K. Lee, Grace Y. Lau, Mayank Sabharwal, Xiong Peng, Michael C. Tucker

Abstract

While the porous-transport layer (PTL) is a key component in PEM electrolyzers, it is one of the most underexplored due to limited available structures. In this work, we present a novel PTL design for PEM water electrolyzers enabled by a cost-effective, scalable tape-casting technique. A precise control of the PTL pore structure is achieved by incorporating poreformers of various sizes, and by varying the titanium and poreformer ratio. The structures are characterized with SEM and synchrotron X-ray computed tomography imaging techniques. Comprehensive electrochemical performance analysis demonstrates that higher titanium loading provides improved contact at the catalyst-layer/PTL interface but suffers from severe mass-transport losses due to gas bubbles. We solve this mass-transport problem by mixing in large poreformer beads that produce a highly porous structure with excellent gas removal properties yet still maintaining mechanical integrity. The PTL fabricated with 60:40 Ti:PMMA ratio and 60 µm PMMA bead size outperformed the standard commercial Ti powder-based PTL by 62 mV at 4 A/cm^2.

Introduction

Hydrogen is an excellent energy vector or carrier with immense potential to realize clean and sustainable energy systems.[1,2] In the transportation sector, hydrogen-based fuel cells may replace heavy-duty diesel combustion engines, which consume 25% of the annually allocated vehicle fuel and contribute 23% of the total carbon dioxide emissions in the United States.[3] Moreover, hydrogen is used as a feedstock for synthesis of many chemicals including ammonia and steel production.[4,5] For instance, annual ammonia production is approximately 200 Mtonne/year and switching to clean hydrogen would curtail CO_2 emissions by 420 Mtonne/year.[4] Shifting towards clean hydrogen, produced without carbon footprint, is essential to achieve decarbonization.

Most of the hydrogen used today is produced via steam-methane reforming processes, which impart a tremendous carbon footprint of approximately 9 kg CO_2 per kg H_2 produced.[6] A promising alternative to the reforming process is electrolysis coupled with renewable energy sources, which can produce hydrogen without carbon emissions.[2,7–9] While various types of electrolyzers are available today, proton-exchange-membrane (PEM) water electrolyzers are the most promising technology for decarbonization, producing high purity hydrogen (99.99%) with rapid response to the supplied power, and therefore suitable for coupling with renewable energy sources. In addition, their compact design and safe operation are advantageous for large-scale applications. One major bottleneck in further adoption of this technology is the high cost, which urgently calls for the need of cost-reduction strategies. One viable solution is to enable high current-density operation, which requires optimization of PEM water electrolyzer components.

Porous-transport layers (PTLs) are crucial components in PEM water electrolyzers that facilitate reactant and product transport in the system including electrons, water, and gases (hydrogen and oxygen).[10–13,14–18] Good interfacial contact at the catalyst layer and PTL (CL/PTL interface) is necessary to achieve high catalyst utilization during water splitting.[14,15,19–21] Hence, CL/PTL interfacial contact and mass-transport

properties are considered to be key parameters of a PTL. Several studies have shown the importance of the CL/PTL interface.[22–24] For instance, Majasan *et al*. observed the impact of titanium microstructure on the CL/PTL interface, where finer microstructure is favored for enhanced contact. Moreover, PTL structure becomes a more dominant factor at lower CL loading.[22,25] Mass transport in the anode compartment has been a major topic of interest recently. *Operando* imaging revealed that oxygen gas removal is crucial to minimize mass-transport losses.[10,12,26–28] Lee *et al*. conducted pore-network modeling on PTLs and determined that larger pores are favored for mass transport, but there exists a tradeoff between mass transport and interfacial contact; while larger pores are required for gas removal, low porosity and small pores are needed for enhanced interfacial contact.[29,30] To overcome this tradeoff, the addition of a backing layer was proposed to improve the CL/PTL interface, yet this requires further optimization.[31–36] Typically, PTLs are fabricated from titanium to withstand the highly corrosive environment of pure oxygen, and this severely limits the availability of PTLs used in the field. Most PTLs are supplied by the filtration industry and are not optimized for electrolysis. Therefore, precise control of the PTL pore structure tailored for water electrolysis– such as controlling pore size diameter in addition to total porosity – is not available at this moment. In this work, we use tape casting to enable precise PTL pore-structure control to understand and optimize PTL properties for water electrolyzers.

Tape casting is an economical and scalable process for creating a variety of substrates, prevalently used for industrial applications in the fabrication of ceramic and metal sheets.[37] Typical tape cast sheet thickness ranges from approximately 5 to 1000 μm, enabling adaptability to a wide range of applications. Tape casting of metal particles has been used to fabricate porous sheets of various metals, including stainless steel and Ni-Fe for solid oxide fuel cell supports[38,39], Cu for heat pipes[40], and Ni for filtration.[41] In addition, the feasibility of using tape casting to fabricate Ti PTLs at an industrial scale with rough and spherical particles has been demonstrated in principle,[42] but not optimized for PEM electrolyzer performance.

In this work, we use tape casting to grasp fundamental understanding of key PTL parameters. We incorporate poreformers (polymethyl methacrylate, PMMA) to tailor the pore structure of the PTL, and control the titanium-to-PMMA ratio to design PTLs with varying CL/PTL interfaces. The structures are analyzed with SEM and synchrotron micro-tomography imaging. We align electrochemical and structural analysis of the fabricated PTLs to suggest an enhanced PTL design specific to the electrolyzer application.

Experimental Methods

Preparation of Titanium Tape

Titanium tape-casting slurries were prepared with commercially-available hydride-dehydride (HDH) titanium powder (Alfa Aesar, -325 mesh) as the starting material. The titanium powder was mixed with 2.5 wt% polyvinyl butryal (PVB, Spectrum Chemical) as a binder, 2.5 wt% polyethylene glycol (Sigma Aldrich, MW 300) as a surfactant, and 30 wt% Ethanol (Sigma Aldrich). To introduce controlled porosity, 40 or 60v% of the Ti was replaced with PMMA poreformer (Sunjin) with particle size of approximately 10, 30 or 60 μm, Figure S1. The slurry was mixed in a utilized jar mill (US Stoneware RMV 755) for 24 h at ambient temperature and pressure.

Casting of tapes from the titanium slurry was conducted on a lab-scale caster (MSK-AFA IIID Automatic Thick Film Coater), preheated at 40°C for 10 minutes. The thickness of the green tapes was adjusted to

300 μm using doctor blade with adjustable gap height (Paul N. Gardner Company, Inc). The slurry was cast on a silicon-treated polyethylene terephthalate (Si-PET) substrate film and dried for 24 hours.

Sintering Titanium Film for PTL Fabrication

The dry titanium tape was removed from the Si-PET film, cut to size, and placed onto a zirconia substrate (MTI Corporation, 8% YSZ Ceramic Substrate). The tape and substrate were loaded into a tube furnace (Lindberg Blue, with alumina tube) under flowing ultra high (99.999%) purity argon. The tape was sintered at 1000°C for 2 h with 3°C/min heating and cooling rates and a 2 h debinding hold at 400°C during ramp up. After sintering, the porous titanium sheet was cut with an optical fiber laser cutter (Full Spectrum Laser) to match the electrolyzer active area (5 cm^2). The prepared PTLs were then cleaned using commercially available etching solution (Multi-etch) and were coated with a layer of platinum at the CL/PTL interface to enhance electrical properties and to prevent formation of oxide layers. Approximately 40 nm layer of Pt was deposited at the CL/PTL interface using RF sputtering (AJA International Inc). The deposition rate was 1.75 Å/s in an Argon environment at 30 mTorr.

Imaging

The morphology of tape casted PTL samples was analyzed using scanning electron microscopy (SEM). PTL samples were mounted in slow-curing transparent epoxy (Struers, EpoFix). The epoxy cured overnight and then samples were cross-sectioned and polished on a metallurgical sample polisher (Buehler). The samples were polished using silicon carbide grinding paper (Struers), with grit sizes 240, 320, 400, 600, 800, and 1200. Then the samples were further polished with water based polycrystalline diamond suspension (3, 1, and 0.05 μm) on polishing cloth (Allied High Technology Products). The polished samples were sputtered with a thin layer of gold for better electronic conductivity. The samples were then loaded to the SEM (JEOL 7500F) for imaging.

X-ray computed tomography (XCT) was performed at the Advanced Light Source (ALS) Beamline 8.3.2 at Lawrence Berkeley National Laboratory with 100% whitebeam with peak energy greater than 50 keV. 1969 projections were collected over a rotation of 180° with an exposure time of 200 ms. Dark field images were collected to deduct detector dark counts with the X-ray shutter closed, and bright field images were collected before and after the sample scan to normalize for variations in the incident illumination. The 3D reconstructions were performed with TomoPy. The reconstructed datasets were segmented using an in-house developed python code which uses a multi-step Otsu thresholding to binarize the grey-scale data. The pore size distribution was computed using a maximal sphere fitting algorithm.[43]

Thermogravimetric Analysis

The change in weight of the titanium powder, poreformer (PMMA) and binder (PEG) as a function of temperature was measured using a thermogravimetric analyzer system (Perkin Elmer, TGA 4000). Each sample (20 mg) was placed in a ceramic crucible and heated to 900°C at a ramp rate of 3°C/min. Ultra-high argon (99.999%, 20 ml/min) was flushed through the sample chamber to mimic the Ti sintering conditions.

Electrolyzer Cell Assembly

Catalyst coated membranes (CCMs) were used for electrolyzer cell testing of the various tape-cast PTLs. Ultrasonic spray coating was used to prepare a fresh CCM for each PTL tested. Commercially-available

iridium oxide catalyst (TKK ECL-0110 SA = 100, Tanaka) was mixed with Nafion ionomer solution (5 wt%, Ion Power D521) at ionomer-to-iridium weight ratio of 0.116 to make catalyst ink for the anode of the electrolyzer. Platinum supported by carbon (TEC10V50E 46.8% Pt, Tanaka) mixed with Nafion ionomer solution (5 wt%, Ion Powder D521) at ionomer-to-catalyst weight ratio of 0.45 was used for the cathode catalyst ink. The content of the catalyst ink and ionomer-to-catalyst ratios were kept constant throughout the study. Nafion membrane with thickness of 178 µm (N117, Ion Power) was used as the PEM for the CCM. Impurities in the membranes were removed by first soaking in boiling DI water for 1 h. Membranes were then protonated by immersing in 0.5 M HNO_3 (ACS Reagent, Sigma-Aldrich) for 1 h at room temperature. The membranes were then rinsed with DI water. A Sono-Tek ultrasonic spray coater with sonication set to 120 kHz was used for CCM fabrication. The membrane was fixed flat on a vacuum plate at constant temperature of 80°C. Catalyst loadings were measured via X-ray fluorescence (XRF) (Bruker M4 Tornado, Bruker). Iridium oxide loading of 0.4 ± 0.02 $mg_{Ir} \cdot cm^{-2}$ was achieved for the anode side, and platinum loading of 0.1 ± 0.01 $mg_{Pt} \cdot cm^{-2}$ was achieved for the cathode side. The active area of the CCMs was 5 cm^2.

A single-cell electrolyzer hardware (Fuel Cell Technology, FCT) equipped with a platinum-coated single parallel channel titanium flow field at the anode and a graphite single channel serpentine flow field at the cathode was used. Tape casted PTLs fabricated with Ti:PMMA volume ratios of 100:0, 60:40, and 40:60, each with PMMA bead sizes of 10, 30, and 60 µm were used as the anode PTL. The baseline PTL was a commercially-available sintered titanium powder-based PTL (Mott 1100 Series, Mott Corp.). The baseline PTL is composed of sintered Grade 2 Ti powders with thickness of 254 µm with porosity of 37%. The cathode gas-diffusion layer was a carbon paper without an MPL (Toray 120) with PTFE content of 5%. Ethylene tetrafluoroethylene (ETFE) gaskets were used to seal the electrolyzer. The thickness of the gasket was chosen to achieve 30% compression in the GDL, and the electrolyzer cell was torqued up to 4.5 Nm.

A multichannel potentiostat (VSP 300, Biologic) with 20 A booster was used to conduct electrochemical tests. A house-modified test station (Fuel Cell Technologies) was used for electrochemical testing. Heated deionized (DI) water flowed into the anode and fully humidified H_2 flowed into the cathode at 100 mL/min. A set of cartridge heaters maintained the electrolyzer temperature at 80°C. Cyclic voltammetry (CV) conditioning (10 cycles at a scan rate of 50 mV/s between 1.2 and 2 V) was implemented before measuring polarization curves and electrochemical impedance. The polarization curve was obtained by holding at various constant cell currents over a period of 130 s, and averaging the last 30 s of the period. Galvanostatic electrochemical-impedance spectroscopy (EIS) was used to measure impedance spectra at each current step of the polarization curve. The frequency ranged from 1 MHz to 100 mHz. The amplitude of the applied AC current was selected for each step to ensure a sufficient signal to noise ratio while maintaining a linear system response. The iridium cyclic voltammetry was measured by cycling cell potential from 0.05 to 1.2 V at scanning rate of 50 mV/s with liquid DI water and fully humidified H_2 flowing anode and cathode, respectively. An applied voltage breakdown analysis was performed on measured polarization curves and impedance spectra as shown from our previous work.[44] the theoretical thermodynamic potential was first calculated, follow by ohmic and kinetic overpotentials. By isolating mass transport overpotential from the total cell potential and overpotentials, we were able to obtain full voltage breakdown curves.

Results and Discussion

Rough Ti particles and PMMA poreformer beads were combined into flexible sheets via tape casting, sintered to produce free-standing porous Ti PTL components, and integrated into PEMWE devices for performance testing, Figure 1. Various aspects of the Ti PTL fabrication process were explored, including sintering conditions, Ti and PMMA particle properties, and poreformer volume loading. The porous Ti structures were imaged with SEM and micro-tomography. PEMWE operation revealed the impact of pore structure on performance.

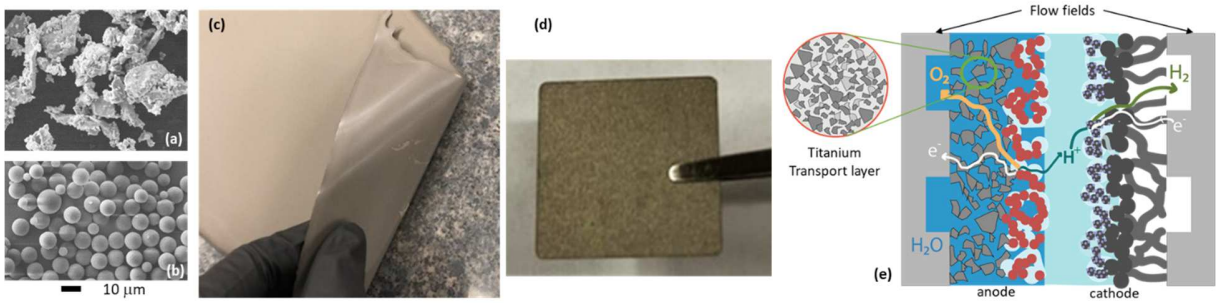

Figure 1. An overview of Ti PTL processing and integration into a PEMWE device. SEM images of (a) rough Ti particles and (b) PMMA poreformer beads. Photographs of (c) a flexible cast tape and (d) a final Ti PTL after sintering. (e) Schematic of a PEMWE showing the placement of the Ti PTL within the multi-layered electrochemical device. (Adapted with permission from Reference 45).[45]

Selection of Tape casting Materials and Sintering Conditions

The goal of tape casting and sintering is to produce a strong, electronically conductive porous Ti sheet that has adequate pore structure for countervailing transport of both liquid water and gaseous oxygen to/from the reaction site. Hydride-dehydride (HDH) Ti particles were chosen, as random packing and mechanical interlocking of such rough particles provide low starting density and excellent mechanical strength in the green state.

Sintering requires good metal-to-metal contact between adjacent particles. It is a common practice to debind cast tapes in air before sintering in a controlled atmosphere. This risks oxidizing the Ti surface to TiO_2, however, which can prevent metal-to-metal contact and impede sintering. Significant oxidation of Ti occurs above about 300°C in air, Figure 2a. To determine the maximum acceptable processing temperature in air, Ti particles were oxidized at various temperatures in air for 1 h, and then sintered in Ar at 1100°C. For oxidation at 400°C and lower, a dense and strong Ti monolith was achieved after sintering, Figure 2b. For oxidation at 450°C and higher, minimal sintering occurred and the Ti was brittle and remained porous, Figure 2c. Complete removal of many common binders in air requires debinding temperature around 500°C or higher,[38,43,44] for example PVB burns out around 550°C, Figure 2a. Therefore, air debinding followed by sintering in Ar is not an effective process for Ti with these binders. One approach to mitigate surface oxidation is to sinter in a highly reducing atmosphere containing hydrogen. This would achieve reduction of surface TiO_2, however concomitant hydriding of Ti leads to hydrogen embrittlement and phase transformation.[46,47]

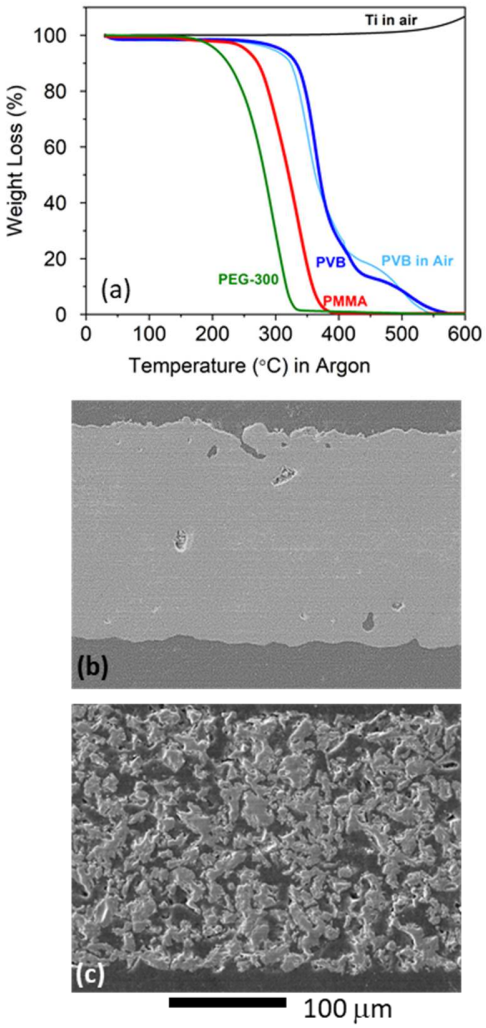

Figure 2. Impact of processing atmosphere. (a) TGA in air for Ti particles (black) and PVB (light blue), and in Ar for PVB (dark blue), PEG-300 (green), and PMMA particles (red). SEM image of polished cross-section of Ti particles sintered at 1100°C (b) directly in Ar and (c) in Ar after debinding in air at 525°C for 1 h.

Another approach is to utilize binders and other tape-casting additives that can be completely removed in Ar at temperatures below the initiation of Ti sintering. Such a process and tape-casting system was previously reported in the literature, and we use it here with some modifications.[42] Tapes were cast from a slurry of Ti particles, PVB binder, PEG-300 dispersant, and ethanol solvent. These specific polymer additives were selected because they are compatible with debinding and sintering in Ar atmosphere, and are completely removed at around 550°C or lower, Figure 2a. Ultra-high-purity Ar was used for sintering, as initial trials indicated that industrial-grade Ar and vacuum atmosphere contained enough residual oxygen to oxidize the Ti surface and impeded sintering. Various maximum sintering temperatures were evaluated, and 1000°C was selected for the next phase of tape development, Figure 3. Incomplete sintering with shrinkage of 8% occurred at 900°C, producing a weak structure. Sintering at 1100 to 1200°C caused over-densification of the Ti. Sintering at 1000°C produced a strong structure with shrinkage of 14%, and was selected as a good tradeoff between strength and retention of porosity.

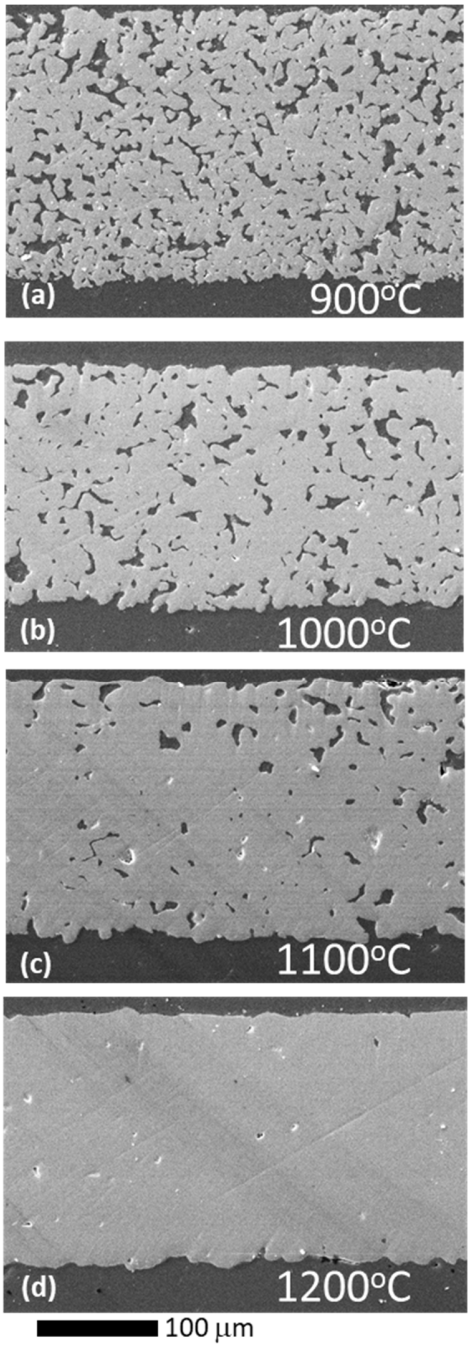

Figure 3. Impact of sintering temperature on Ti structure. SEM images of polished cross-sections of Ti tapes sintered at (a) 900°C, (b) 1000°C, (c) 1100°C, and (d) 1200°C.

Poreformer Optimization

Ti PTLs with varying pore size have been produced from different sizes of sintered particles, with larger particles producing larger pores.[48] Previous Ti PTL tape-casting effort used slurries with only Ti particles and soluble polymer additives.[42] Here, poreformer beads are added to manipulate the pore structure of the sintered Ti PTL. Cross-linked PMMA beads were chosen because they are widely used as a poreformer

in the fabrication of ceramic and metal structures,[49,50] do not swell in solvents, and are fugitive in Ar below 400°C (see Figure 2a). PMMA is much less dense than Ti, so buoyancy separation of PMMA and Ti during casting and drying is a concern. Heating the casting bed moderately to 40°C increased the tape drying speed, allowing less time for separation before the solvent was evaporated. Heating noticeably improved homogeneity of the poreformer distribution in the tape relative to casting onto an un-heated bed, and was therefore used for all subsequent castings. Various poreformer sizes were evaluated. The poreformer particles have a relatively wide particle-size distribution (see Figure S1), and nominal average sizes in μm are used here to label each type. PMMA-100 particles separated from the Ti particles during tape drying, despite heating the casting bed, and were therefore eliminated from further consideration (see Figure S2). PMMA-10, PMMA-30, and PMMA-60 did not separate.

PMMA-10, PMMA-30, and PMMA-60 were mixed with Ti at various Ti:PMMA volume loading ratios. For 20:80 ratio, the resulting sintered PTL was very weak and did not survive handling during further processing. Strong PTLs were achieved for 40:60 and 60:40 ratios. For these structures, samples were cross-sectioned and imaged with SEM, Figure 4. Selected samples (60:40 Ti:PMMA) were also characterized with synchrotron x-ray tomography, Figures 5 and S3. The pore sizes follow the expected trend (Figures 4 and 5a). The larger poreformers produce a wide range of pore size, due to the inhomogeneous distribution of PMMA particle size (Fig S1), and retention of small residual pores between Ti particles where no poreformer beads are present, as clearly seen for 100:0 Ti:PMMA (Fig 4h). Note also that the pores shrink during sintering. The poreformers appear to be well-dispersed throughout the cross-section of the PTLs. The top and bottom surfaces of the structures are generally slightly less porous than the faces, Fig 5b and Figure S3. All Ti PTLs fabricated here are approximately 200 μm thick. This is a similar thickness to previous tapecast Ti PTLs, but significantly thinner than the typical 1 to 1.4 mm thickness for sintered Ti powder.[48] The chemical composition of the fabricated PTL has been analyzed via SEM-EDX, and the titanium is found to be high purity (Figure S4). Titanium peaks dominate the EDX spectra of the sintered PTL. Trace Si may be observed around 1.7 keV, but it is below the threshold for unambiguous detection by SEM-EDX. Observed gold peaks refer to the gold coating sputtered onto the sample during the SEM sample preparation.

A poreformer-free baseline PTL was also prepared, and its structure was quite dense as expected, Figure 4h. A commercial Ti PTL with similar thickness was also used as a baseline, Figure 4i. The commercial material appears to be fabricated by tape casting or powder bed sintering, without any poreformer added.

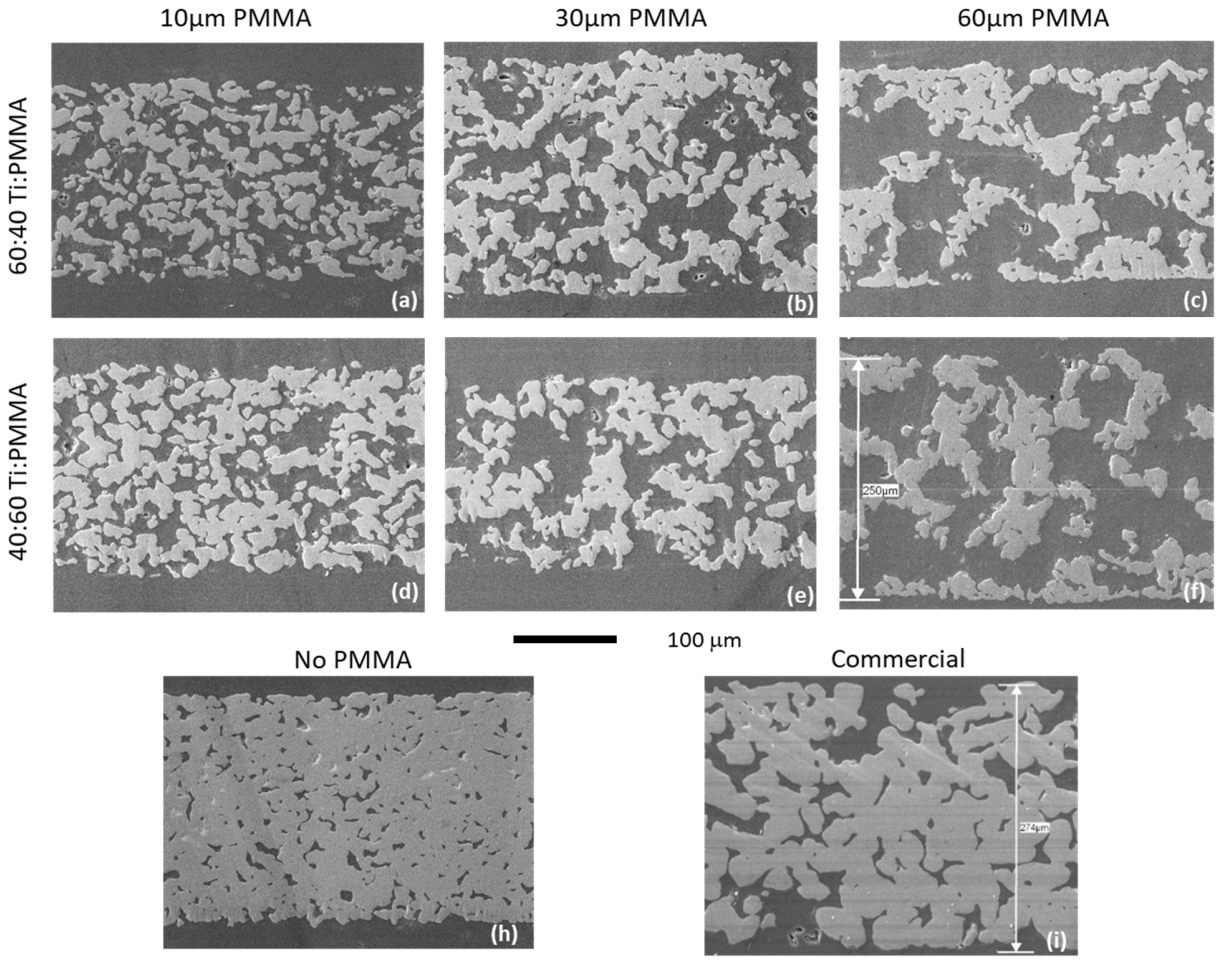

Figure 4. Ti PTL structures. SEM images of polished cross-sections of sintered PTLs prepared with (a,d) PMMA-10, (b,e) PMMA-30, or (c,f) PMMA-60 at Ti:PMMA volume loading ratios of (a-c) 40:60 or (d-f) 60:40. (h) PMMA-free and (i) commercial PTLs are show for comparison.

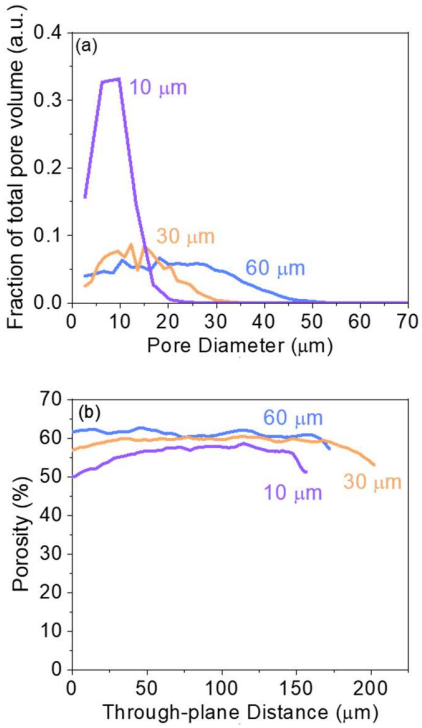

Figure 5. Tomography characterization of 60:40 Ti:PMMA. (a) Pore size distribution in the entire imaged volume. (b) Local porosity through the thickness of the sample in the imaged volume.

Electrochemical testing

Controlling the Ti:PMMA loading ratio and PMMA bead size enables fine tuning of pore structure in the PTL. Here, we investigate the impact of PTL pore structure on electrolyzer performance via a series of electrochemical analyses. Specifically, we seek to observe the impact on interfacial contact at the CL/PTL interface and on mass transport arising from: (*i*) enlarged pore diameters by increasing PMMA particle size, and (*ii*) titanium phase volume fraction by varying the PMMA loading ratio. The polarization curves and overpotential breakdowns for Ti:PMMA ratios of 40:60 and 60:40 are as shown in Figure 6. For 40:60 ratio, 10 µm PMMA size exhibits the lowest overpotentials up to 3 A/cm^2, above which there is a significant increase in mass-transport overpotential. For 40:60 Ti:PMMA ratio, 10 µm PMMA particles provide relatively better CL/PTL interfacial contact area compared to larger PMMA particles, see Figure 4. This leads to improved kinetics and higher catalyst utilization (Figure S5), which dominate during electrolysis at low current density. However, at higher current density, where the rate of gas generation substantially increases, the pore structure formed by 10 µm PMMA beads is insufficient for gas removal, resulting in higher mass-transport overpotential. We observe a trend of higher electrolyzer efficiency with increasing PMMA bead sizes above ~3 A/cm^2 for 40:60 TI:PMMA ratio. A similar trend holds for the Ti:PMMA ratio of 60:40, although the PTL with 60 µm PMMA bead size outperforms other bead sizes throughout the entire range of current density. The 60:40 ratio with higher loading of Ti provides more homogeneous contact at the CL/PTL interface. Hence, the kinetics and catalyst utilization are improved relative to the PTLs fabricated with the 40:60 ratio at all PMMA bead sizes.[14] Similarly, the ohmic overpotentials from 60:40 ratio outperforms that of 40:60. We observe that within 60:40 ratio PTLs, larger bead sizes (from 10 to 60 µm) increase ohmic overpotential by 101 mV at 4 A/cm^2. This is attributed to the compromised

interfacial contact with the increased PMMA bead size. Interestingly, mass-transport losses are exacerbated for both 10 and 30 µm PMMA size for the 60:40 ratio, but only for 10 µm PMMA size for the 40:60 ratio. This is because the 60:40 ratio PTLs are denser, requiring larger pore sizes to evacuate gaseous oxygen generated. Our results are experimentally in agreement with previous modeling studies that found pore size to be a critical parameter for facilitating gas removal.[29,30] Currently for Ti powder-based PTLs, a precision control over pore diameters is severely limited – solely relying on varying titanium powder diameters and porosities. The proposed fabrication method of tape casting with the addition of pore formers provides scalable and groundbreaking solution to commercial PTL designs specific for PEM electrolysis.

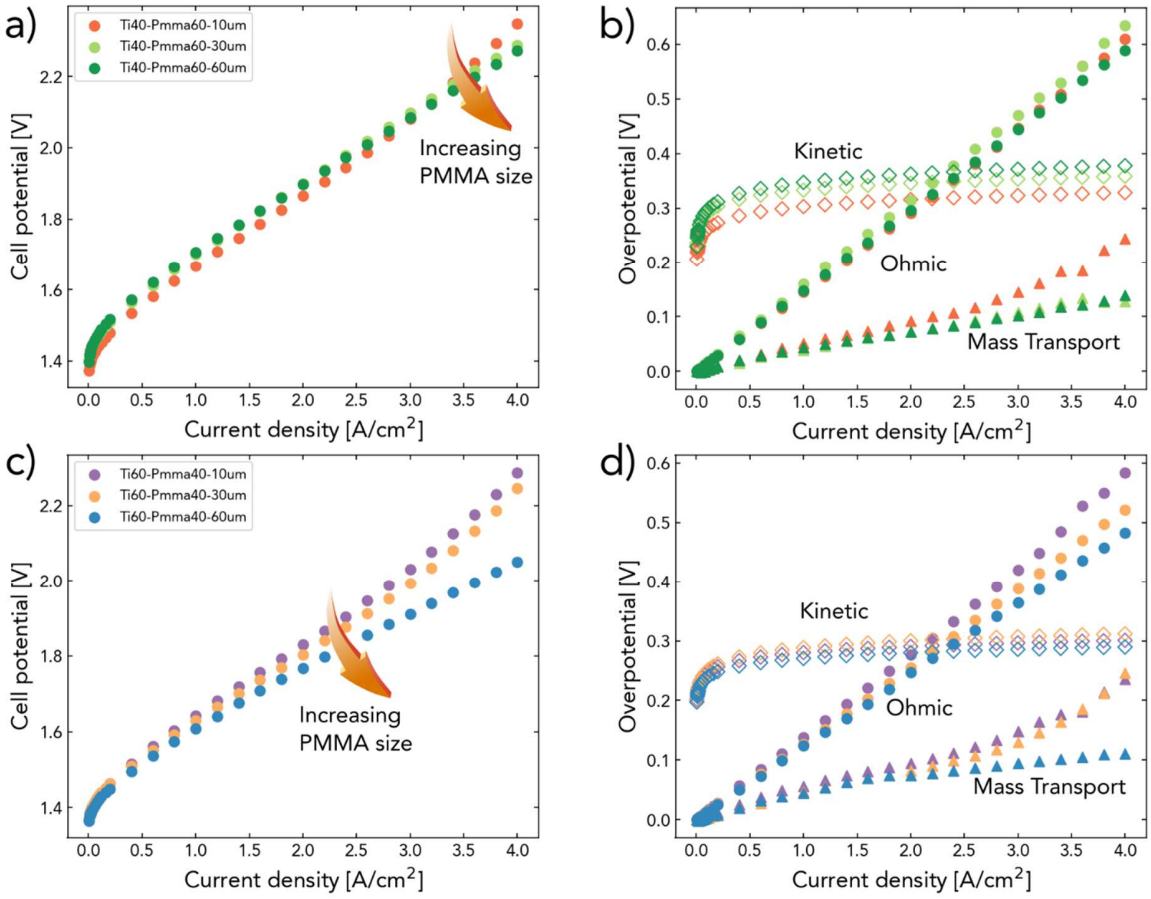

Figure 6. Impact of PMMA particle size. (a,c) Polarization curves and (b,d) overpotential breakdowns for (a,b) 40:60 Ti:PMMA tape casted PTLs, and (c,d) 60:40 Ti:PMMA tape casted PTLs. Increasing particle size of the PMMA decreases mass transport overpotentials at high current density. The electrolyzer operated under operating condition of atmospheric pressure at 80 °C with liquid water flow rate of 100 mL/min.

The impact of Ti:PMMA ratio on electrolyzer performance was further investigated. The polarization curves and overpotential breakdowns for PTLs with Ti loadings of 40%, 60%, and 100%, and for a commercial PTL are shown in Figure 7. The 60:40 Ti:PMMA PTL demonstrates outstanding performance, which outperforms the commercial PTL throughout the range of operating current density. At lower Ti loading (40:60 Ti:PMMA), the PTL provides poor contact against the catalyst layer, leading to higher ohmic and kinetic overpotentials and eventually inferred lower catalyst utilization. At the highest Ti loading (no

PMMA), the PTL exhibits low ohmic and kinetic overpotentials at low current density, but shows a rapid increase in ohmic and mass-transport overpotentials at current densities above 1 A/cm^2. This is due to a buildup of oxygen gas at the CL/PTL interface that reduces the participation of reaction sites. Specifically, the 100:0 Ti:PMMA PTL has almost no pores (see Fig 4h) and the increased rate of gas generation at high current density floods the interface with gas. As a result, severe gas accumulation dehydrates the catalyst coated membrane, increasing high-frequency resistance and mass-transport overpotential, as seen in Figure 7b. These behaviors are consistent to the dehydration effects observed previously in the literature.[51,52]

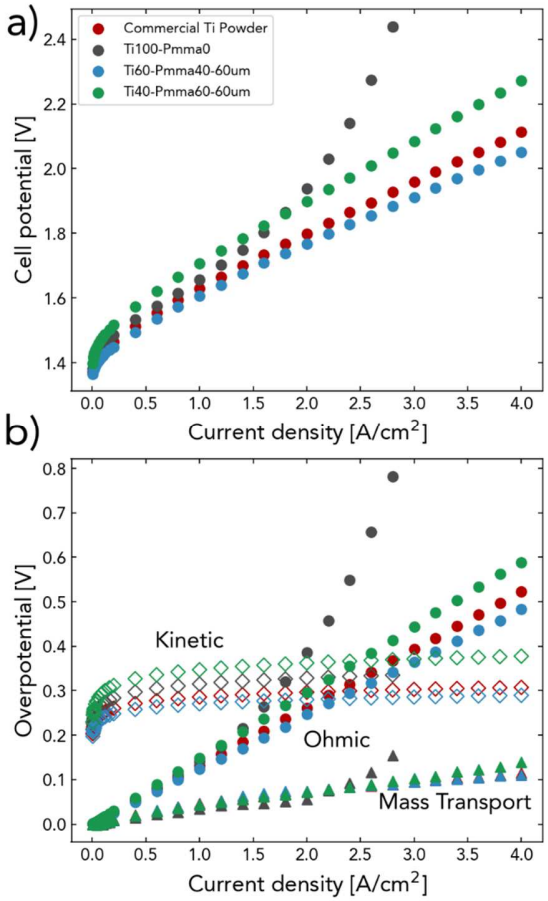

Figure 7. Impact of Ti:PMMA loading. (a) Polarization curves and (b) overpotential breakdowns for PTLs with varying Ti:PMMA ratio, with PMMA particle size held constant at 60 µm. Ti:PMMA ratio of 60:40, with improved ohmic and kinetic properties, outperforms the commercially available sintered Ti PTL. The electrolyzer operated under operating condition of atmospheric pressure at 80 °C with liquid water flow rate of 100 mL/min.

The impact of PTL pore structure on electrolyzer performance was also analyzed with galvanostatic EIS. The EIS measurements are conducted separately after measuring polarization curves. The commercial Ti PTL exhibits significantly lower high-frequency resistance compared to PTLs fabricated from 40:60 and 100:0 Ti:PMMA ratios (Figure 8a). The commercial PTL also has much lower polarization resistance at high current density (Figure 8b) when compared against 40:60 and 100:0 Ti:PMMA ratios. The 100:0 Ti:PMMA PTL demonstrates a dramatic increase in high-frequency and polarization resistances consistent with the

dehydration effects observed from polarization curves. In contrast, PTLs fabricated with 60:40 Ti:PMMA show improved high-frequency and polarization resistances (Figure 8c and d). In particular, the 60 um PMMA bead sized PTL have lower high-frequency resistance as well as polarization resistances compared to the commercial PTL, which is attributed to improved CL/PTL contact. However, for PMMA bead sizes of 10 and 30 µm, notably higher polarization resistance is observed at elevated current density, suggesting insufficient pore space for gas removal.

Overall, the tape casted PTL with a ratio of 60:40 Ti:PMMA with 60 µm PMMA size is found to be the best PTL among those tested, due to a balanced tradeoff between gas removal and sufficient interfacial contact. Our results reveal that both the volume fraction of titanium phase in the PTL and the actual diameter of the pore openings are crucial to electrolyzer performance, and fine tuning of the pore size and titanium weight percentage is required for optimization. Addition of poreformer did not compromise the mechanical integrity of the PTL, and it did not deform under the cell compression load as the post-operation structure and thickness of the optimized sample was found to be the same as the as-sintered structure (Figure S6).

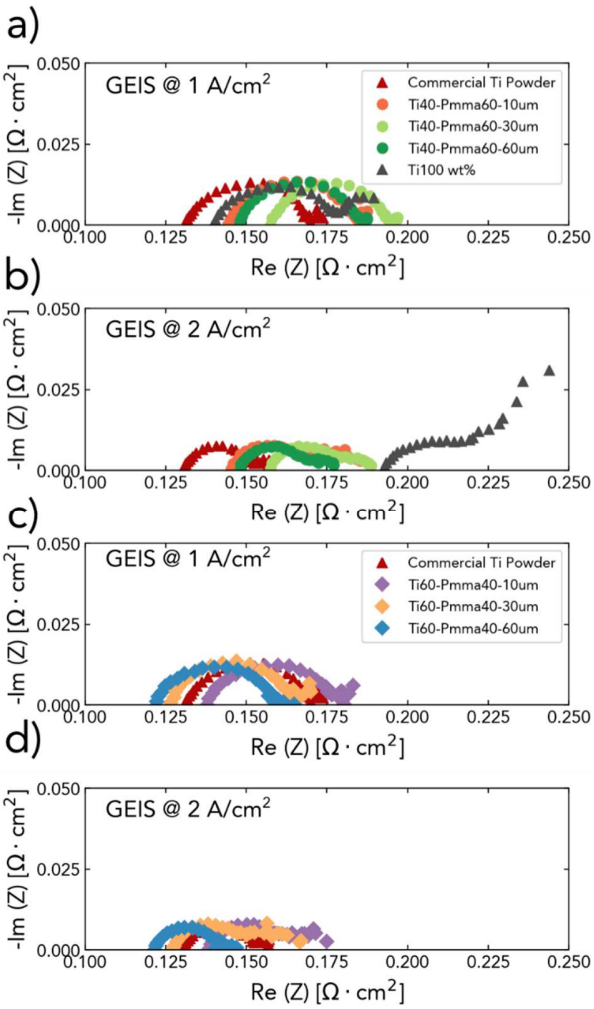

Figure 8. EIS. Galvanostatic electrochemical impedance spectroscopy measurements for (a and b) 40:60 Ti:PMMA tape casted PTLs, and (c and d) 60:40 Ti:PMMA tape casted PTLs. Increase in mass transport overpotential is prominently observed for PTLs with smaller particulate size of PMMA.

Conclusions

This work provides valuable insight into the porous-transport-layer (PTL) design for commercialization and wide adoption of PEM water electrolyzers. We achieve precise control of the PTL pore structure through tape casting. Specifically, poreformers were incorporated to tailor the pore structure, and the titanium-to-poreformer ratio was controlled to fabricate PTLs with specific structural properties. Comprehensive electrochemical analysis indicates that higher titanium loading is desired to achieve improved contact at the catalyst layer/PTL interface. Higher titanium loading alone leads to severe mass-transport issues, but we demonstrate that the addition of large poreformer beads increases performances due to expected gas-removal enhancement.. Through this fabrication method, a PTL formed from 60:40 Ti:PMMA with 60 μm PMMA outperforms a standard commercial Ti powder-based PTL up to 62 mV at 4 A/cm^2.

Acknowledgements

We thank Dr. Nem Danliovic for suggesting this work and helpful discussion. The authors acknowledge the Department of Energy–Office of Energy Efficiency and Renewable Energy–Fuel Cell Technologies Office (DOE-EERE-FCTO) and the H2 from the Next-generation Electrolyzers of Water (H2NEW) consortium for funding under Contract Number DE-AC02-05CH11231. This research used resources of the Advanced Light Source (ALS), a DOE Office of Science User Facility under contract no. DEAC02-05CH11231. We are grateful to Dr. Dula Parkinson for help with micro-tomography measurement at Beamline 8.3.2 of ALS.

References

(1) Oliveira, A. M.; Beswick, R. R.; Yan, Y. A Green Hydrogen Economy for a Renewable Energy Society. *Curr Opin Chem Eng* **2021**, *33*, 100701. https://doi.org/10.1016/J.COCHE.2021.100701.

(2) Ayers, K.; Danilovic, N.; Ouimet, R.; Carmo, M.; Pivovar, B.; Bornstein, M. Perspectives on Low-Temperature Electrolysis and Potential for Renewable Hydrogen at Scale. *https://doi.org/10.1146/annurev-chembioeng-060718-030241* **2019**, *10*, 219–239. https://doi.org/10.1146/ANNUREV-CHEMBIOENG-060718-030241.

(3) Cullen, D. A.; Neyerlin, K. C.; Ahluwalia, R. K.; Mukundan, R.; More, K. L.; Borup, R. L.; Weber, A. Z.; Myers, D. J.; Kusoglu, A. New Roads and Challenges for Fuel Cells in Heavy-Duty Transportation. *Nature Energy 2021 6:5* **2021**, *6* (5), 462–474. https://doi.org/10.1038/s41560-021-00775-z.

(4) Nayak-Luke, R.; Bañares-Alcántara, R.; Wilkinson, I. "green" Ammonia: Impact of Renewable Energy Intermittency on Plant Sizing and Levelized Cost of Ammonia. *Ind Eng Chem Res* **2018**, *57* (43), 14607–14616. https://doi.org/10.1021/ACS.IECR.8B02447/ASSET/IMAGES/LARGE/IE-2018-02447Z_0007.JPEG.

(5) Muslemani, H.; Liang, X.; Kaesehage, K.; Ascui, F.; Wilson, J. Opportunities and Challenges for Decarbonizing Steel Production by Creating Markets for 'Green Steel' Products. *J Clean Prod* **2021**, *315*, 128127. https://doi.org/10.1016/J.JCLEPRO.2021.128127.

(6) Ali Khan, M. H.; Daiyan, R.; Neal, P.; Haque, N.; MacGill, I.; Amal, R. A Framework for Assessing Economics of Blue Hydrogen Production from Steam Methane Reforming Using Carbon Capture Storage & Utilisation. *Int J Hydrogen Energy* **2021**, *46* (44), 22685–22706. https://doi.org/10.1016/J.IJHYDENE.2021.04.104.

(7) Carmo, M.; Fritz, D. L.; Mergel, J.; Stolten, D. A Comprehensive Review on PEM Water Electrolysis. *International Journal of Hydrogen Energy*. Pergamon April 22, 2013, pp 4901–4934. https://doi.org/10.1016/j.ijhydene.2013.01.151.

(8) Shirvanian, P.; van Berkel, F. Novel Components in Proton Exchange Membrane Water Electrolyzers (PEMWE): Status, Challenges and Future Needs. *Electrochemistry Communications*. Elsevier Inc. May 1, 2020, p 106704. https://doi.org/10.1016/j.elecom.2020.106704.

(9) Grigoriev, S. A.; Porembsky, V. I.; Fateev, V. N. Pure Hydrogen Production by PEM Electrolysis for Hydrogen Energy. *Int J Hydrogen Energy* **2006**, *31* (2), 171–175. https://doi.org/10.1016/j.ijhydene.2005.04.038.

(10) Lee, CH.; Lee, J. K.; Zhao, B.; Fahy, K. F.; Bazylak, A. Transient Gas Distribution in Porous Transport Layers of Polymer Electrolyte Membrane Electrolyzers. *J Electrochem Soc* **2020**, *167* (2), 024508. https://doi.org/10.1149/1945-7111/ab68c8.

(11) Angelis, S. D.; Tobias Schuler; A. Charalambous, M.; Federica Marone; J. Schmidt, T.; N. Büchi, F. Unraveling Two-Phase Transport in Porous Transport Layer Materials for Polymer Electrolyte Water Electrolysis. *J Mater Chem A Mater* **2021**. https://doi.org/10.1039/D1TA03379D.

(12) Lee, J. K.; Lee, C.; Fahy, K. F.; Zhao, B.; LaManna, J. M.; Baltic, E.; Jacobson, D. L.; Hussey, D. S.; Bazylak, A. Critical Current Density as a Performance Indicator for Gas-Evolving Electrochemical Devices. *Cell Rep Phys Sci* **2020**, *1* (8), 100147. https://doi.org/10.1016/j.xcrp.2020.100147.

(13) Bazylak, A.; Lee, J. K.; Lee, C. H.; Fahy, K. F.; Kim, P. J.; Krause, K.; LaManna, J. M.; Baltic, E.; Jacobson, D. L.; Hussey, D. S. Accelerating Bubble Detachment in Porous Transport Layers

with Patterned Through-Pores. *ACS Appl Energy Mater* **2020**, *3* (10), 9676–9684. https://doi.org/10.1021/acsaem.0c01239.

(14) Schuler, T.; Schmidt, T. J.; Büchi, F. N. Polymer Electrolyte Water Electrolysis: Correlating Performance and Porous Transport Layer Structure: Part II. Electrochemical Performance Analysis. *J Electrochem Soc* **2019**, *166* (10), F555–F565. https://doi.org/10.1149/2.1241908jes.

(15) Schuler, T.; de Bruycker, R.; Schmidt, T. J.; Büchi, F. N. Polymer Electrolyte Water Electrolysis: Correlating Porous Transport Layer Structural Properties and Performance: Part I. Tomographic Analysis of Morphology and Topology. *J Electrochem Soc* **2019**, *166* (4), F270–F281. https://doi.org/10.1149/2.0561904jes.

(16) Kim, P. J.; Lee, J. K.; Lee, C. H.; Fahy, K. F.; Shrestha, P.; Krause, K.; Shafaque, H. W.; Bazylak, A. Tailoring Catalyst Layer Interface with Titanium Mesh Porous Transport Layers. *Electrochim Acta* **2021**, *373*, 137879. https://doi.org/10.1016/J.ELECTACTA.2021.137879.

(17) Mo, J.; Kang, Z.; Retterer, S. T.; Cullen, D. A.; Toops, T. J.; Green, J. B.; Mench, M. M.; Zhang, F. Y. Discovery of True Electrochemical Reactions for Ultrahigh Catalyst Mass Activity in Water Splitting. *Sci Adv* **2016**, *2* (11). https://doi.org/10.1126/sciadv.1600690.

(18) Borgardt, E.; Panchenko, O.; Hackemüller, F. J.; Giffin, J.; Bram, M.; Müller, M.; Lehnert, W.; Stolten, D. Mechanical Characterization and Durability of Sintered Porous Transport Layers for Polymer Electrolyte Membrane Electrolysis. *J Power Sources* **2018**, *374* (November 2017), 84–91. https://doi.org/10.1016/j.jpowsour.2017.11.027.

(19) Kang, Z.; Mo, J.; Yang, G.; Retterer, S. T.; Cullen, D. A.; Toops, T. J.; Green, J. B.; Mench, M. M.; Zhang, F. Y. Investigation of Thin/Well-Tunable Liquid/Gas Diffusion Layers Exhibiting Superior Multifunctional Performance in Low-Temperature Electrolytic Water Splitting. *Energy Environ Sci* **2017**, *10* (1), 166–175. https://doi.org/10.1039/c6ee02368a.

(20) Mo, J.; Kang, Z.; Yang, G.; Retterer, S. T.; Cullen, D. A.; Toops, T. J.; Green, J. B.; Zhang, F. Y. Thin Liquid/Gas Diffusion Layers for High-Efficiency Hydrogen Production from Water Splitting. *Appl Energy* **2016**, *177*, 817–822. https://doi.org/10.1016/j.apenergy.2016.05.154.

(21) Leonard, E.; Shum, A. D.; Danilovic, N.; Capuano, C.; Ayers, K. E.; Pant, L. M.; Weber, A. Z.; Xiao, X.; Parkinson, D. Y.; Zenyuk, I. v. Interfacial Analysis of a PEM Electrolyzer Using X-Ray Computed Tomography. *Sustain Energy Fuels* **2020**, *4* (2), 921–931. https://doi.org/10.1039/C9SE00364A.

(22) Lopata, J.; Kang, Z.; Young, J.; Bender, G.; Weidner, J. W.; Shimpalee, S. Effects of the Transport/Catalyst Layer Interface and Catalyst Loading on Mass and Charge Transport Phenomena in Polymer Electrolyte Membrane Water Electrolysis Devices. *J Electrochem Soc* **2020**, *167* (6), 064507. https://doi.org/10.1149/1945-7111/ab7f87.

(23) Lickert, T.; Kiermaier, M. L.; Bromberger, K.; Ghinaiya, J.; Metz, S.; Fallisch, A.; Smolinka, T. On the Influence of the Anodic Porous Transport Layer on PEM Electrolysis Performance at High Current Densities. *Int J Hydrogen Energy* **2020**, *45* (11), 6047–6058. https://doi.org/10.1016/j.ijhydene.2019.12.204.

(24) Majasan, J. O.; Iacoviello, F.; Shearing, P. R.; Brett, D. J. L. Effect of Microstructure of Porous Transport Layer on Performance in Polymer Electrolyte Membrane Water Electrolyser. *Energy Procedia* **2018**, *151*, 111–119. https://doi.org/10.1016/j.egypro.2018.09.035.

(25) Peng, X.; Satjaritanun, P.; Taie, Z.; Wiles, L.; Keane, A.; Capuano, C.; Zenyuk, I. v.; Danilovic, N. Insights into Interfacial and Bulk Transport Phenomena Affecting Proton Exchange Membrane Water Electrolyzer Performance at Ultra-Low Iridium Loadings. *Advanced Science* **2021**, *8* (21). https://doi.org/10.1002/ADVS.202102950.

(26) Leonard, E.; Shum, A. D.; Normile, S.; Sabarirajan, D. C.; Yared, D. G.; Xiao, X.; Zenyuk, I. v. Operando X-Ray Tomography and Sub-Second Radiography for Characterizing Transport in Polymer Electrolyte Membrane Electrolyzer. *Electrochim Acta* **2018**, *276*, 424–433. https://doi.org/10.1016/j.electacta.2018.04.144.

(27) Zlobinski, M.; Schuler, T.; Schmidt, T. J.; Buchi, F. N.; Boillat, P. Elucidation of Fluid Streamlining in Multi-Layered Porous Transport Layers ForPolymer Electrolyte Water Electrolyzers by Operando Neutron Radiography. *J Electrochem Soc* **2020**. https://doi.org/10.1149/1945-7111/abcf19.

(28) Panchenko, O.; Giesenberg, L.; Borgardt, E.; Zwaygardt, W.; Kardjilov, N.; Markötter, H.; Arlt, T.; Manke, I.; Müller, M.; Stolten, D.; Lehnert, W.; Panchenko, O.; Giesenberg, L.; Borgardt, E.; Zwaygardt, W.; Kardjilov, N.; Markötter, H.; Arlt, T.; Manke, I.; Müller, M.; Stolten, D.; Lehnert, W. Influence of Stoichiometry on the Two-Phase Flow Behavior of Proton Exchange Membrane Electrolyzers. *Energies (Basel)* **2019**, *12* (3), 350. https://doi.org/10.3390/en12030350.

(29) Lee, J. K.; Lee, C. H.; Bazylak, A. Pore Network Modelling to Enhance Liquid Water Transport through Porous Transport Layers for Polymer Electrolyte Membrane Electrolyzers. *J Power Sources* **2019**, *437*, 226910. https://doi.org/10.1016/j.jpowsour.2019.226910.

(30) Lee, J. K.; Bazylak, A. Optimizing Porous Transport Layer Design Parameters via Stochastic Pore Network Modelling: Reactant Transport and Interfacial Contact Considerations. *J Electrochem Soc* **2020**, *167* (1), 013541. https://doi.org/10.1149/1945-7111/ab6557.

(31) Lettenmeier, P.; Kolb, S.; Burggraf, F.; Gago, A. S.; Friedrich, K. A. Towards Developing a Backing Layer for Proton Exchange Membrane Electrolyzers. *J Power Sources* **2016**, *311*, 153–158. https://doi.org/10.1016/j.jpowsour.2016.01.100.

(32) Lettenmeier, P.; Kolb, S.; Sata, N.; Fallisch, A.; Zielke, L.; Thiele, S.; S Gago, cde A.; Friedrich af, K. A. Energy & Environmental Science Comprehensive Investigation of Novel Pore-Graded Gas Diffusion Layers for High-Performance and Cost-Effective Proton Exchange Membrane Electrolyzers †. *Energy Environ. Sci* **2017**, *10*, 2521. https://doi.org/10.1039/c7ee01240c.

(33) Schuler, T.; Ciccone, J. M.; Krentscher, B.; Marone, F.; Peter, C.; Schmidt, T. J.; Büchi, F. N. Hierarchically Structured Porous Transport Layers for Polymer Electrolyte Water Electrolysis. *Adv Energy Mater* **2020**, *10* (2), 1903216. https://doi.org/10.1002/aenm.201903216.

(34) Lee, J. K.; Lee, C. H.; Fahy, K. F.; Kim, P. J.; LaManna, J. M.; Baltic, E.; Jacobson, D. L.; Hussey, D. S.; Stiber, S.; Gago, A. S.; Friedrich, K. A.; Bazylak, A. Spatially Graded Porous Transport Layers for Gas Evolving Electrochemical Energy Conversion: High Performance Polymer Electrolyte Membrane Electrolyzers. *Energy Convers Manag* **2020**, *226*, 113545. https://doi.org/10.1016/J.ENCONMAN.2020.113545.

(35) Stiber, S.; Balzer, H.; Wierhake, A.; Wirkert, F. J.; Roth, J.; Rost, U.; Brodmann, M.; Lee, J. K.; Bazylak, A.; Waiblinger, W.; Gago, A. S.; Friedrich, K. A. Porous Transport Layers for Proton Exchange Membrane Electrolysis Under Extreme Conditions of Current Density, Temperature, and Pressure. *Adv Energy Mater* **2021**, *11* (33), 2100630. https://doi.org/10.1002/AENM.202100630.

(36) Stiber, S.; Sata, N.; Morawietz, T.; Ansar, S. A.; Jahnke, T.; Lee, J. K.; Bazylak, A.; Fallisch, A.; Gago, A. S.; Friedrich, K. A. A High-Performance, Durable and Low-Cost Proton Exchange Membrane Electrolyser with Stainless Steel Components. *Energy Environ Sci* **2022**, *15* (1), 109–122. https://doi.org/10.1039/D1EE02112E.

(37) Nishihora, R. K.; Rachadel, P. L.; Quadri, M. G. N.; Hotza, D. Manufacturing Porous Ceramic Materials by Tape Casting—A Review. *J Eur Ceram Soc* **2018**, *38* (4), 988–1001. https://doi.org/10.1016/J.JEURCERAMSOC.2017.11.047.

(38) Tucker, M. C. Development of High Power Density Metal-Supported Solid Oxide Fuel Cells. *Energy Technology* **2017**, *5* (12), 2175–2181. https://doi.org/10.1002/ENTE.201700242.

(39) Li, K.; Wang, X.; Jia, L.; Yan, D.; Pu, J.; Chi, B.; Jian, L. High Performance Ni–Fe Alloy Supported SOFCs Fabricated by Low Cost Tape Casting-Screen Printing-Cofiring Process. *Int J Hydrogen Energy* **2014**, *39* (34), 19747–19752. https://doi.org/10.1016/J.IJHYDENE.2014.09.146.

(40) Ru, J.; Kong, B.; Zhu, H.; Shi, Z.; Zhang, D.; Fan, T. Microstructure, Capillary Performance and Gas Permeability of Biporous Copper Fabricated by Tape Casting. *Powder Technol* **2014**, *256*, 182–187. https://doi.org/10.1016/J.POWTEC.2014.02.009.

(41) Liu, W.; Canfield, N. Development of Thin Porous Metal Sheet as Micro-Filtration Membrane and Inorganic Membrane Support. *J Memb Sci* **2012**, *409–410*, 113–126. https://doi.org/10.1016/J.MEMSCI.2012.03.041.

(42) Hackemüller, F. J.; Borgardt, E.; Panchenko, O.; Müller, M.; Bram, M. Manufacturing of Large-Scale Titanium-Based Porous Transport Layers for Polymer Electrolyte Membrane Electrolysis by Tape Casting. *Adv Eng Mater* **2019**, *21* (6), 1801201. https://doi.org/10.1002/ADEM.201801201.

(43) Sabharwal, M.; Pant, L. M.; Putz, A.; Susac, D.; Jankovic, J.; Secanell, M. Analysis of Catalyst Layer Microstructures: From Imaging to Performance. *Fuel Cells* **2016**, *16* (6), 734–753. https://doi.org/10.1002/FUCE.201600008.

(44) Taie, Z.; Peng, X.; Kulkarni, D.; Zenyuk, I. v.; Weber, A. Z.; Hagen, C.; Danilovic, N. Pathway to Complete Energy Sector Decarbonization with Available Iridium Resources Using Ultralow Loaded Water Electrolyzers. *ACS Appl Mater Interfaces* **2020**, *12* (47), 52701–52712. https://doi.org/10.1021/ACSAMI.0C15687/ASSET/IMAGES/MEDIUM/AM0C15687_M006.GIF.

(45) Fornaciari, J. C.; Gerhardt, M. R.; Zhou, J.; Regmi, Y. N.; Danilovic, N.; Bell, A. T.; Weber, A. Z. The Role of Water in Vapor-Fed Proton-Exchange-Membrane Electrolysis. *J Electrochem Soc* **2020**, *167* (10), 104508. https://doi.org/10.1149/1945-7111/AB9B09.

(46) Qian, M.; Schaffer, G. B.; Bettles, C. J. Sintering of Titanium and Its Alloys. *Sintering of Advanced Materials* **2010**, 324–355. https://doi.org/10.1533/9781845699949.3.324.

(47) Fang, Z. Z.; Sun, P.; Wang, H. Hydrogen Sintering of Titanium to Produce High Density Fine Grain Titanium Alloys. *Adv Eng Mater* **2012**, *14* (6), 383–387. https://doi.org/10.1002/ADEM.201100269.

(48) Yuan, X. Z.; Shaigan, N.; Song, C.; Aujla, M.; Neburchilov, V.; Kwan, J. T. H.; Wilkinson, D. P.; Bazylak, A.; Fatih, K. The Porous Transport Layer in Proton Exchange Membrane Water Electrolysis: Perspectives on a Complex Component. *Sustain Energy Fuels* **2022**, *6* (8), 1824–1853. https://doi.org/10.1039/D2SE00260D.

(49) Zhao, B.; Gain, A. K.; Ding, W.; Zhang, L.; Li, X.; Fu, Y. A Review on Metallic Porous Materials: Pore Formation, Mechanical Properties, and Their Applications. *The International Journal of Advanced Manufacturing Technology 2017 95:5* **2017**, *95* (5), 2641–2659. https://doi.org/10.1007/S00170-017-1415-6.

(50) Sarikaya, A.; Dogan, F. Effect of Various Pore Formers on the Microstructural Development of Tape-Cast Porous Ceramics. *Ceram Int* **2013**, *39* (1), 403–413. https://doi.org/10.1016/J.CERAMINT.2012.06.041.

(51) Fornaciari, J. C.; Gerhardt, M. R.; Zhou, J.; Regmi, Y. N.; Danilovic, N.; Bell, A. T.; Weber, A. Z. The Role of Water in Vapor-Fed Proton-Exchange-Membrane Electrolysis. *J Electrochem Soc* **2020**, *167* (10), 104508. https://doi.org/10.1149/1945-7111/AB9B09.
(52) Fornaciari, J. C.; Garg, S.; Peng, X.; Regmi, Y. N.; Weber, A. Z.; Danilovic, N. Performance and Durability of Proton Exchange Membrane Vapor-Fed Unitized Regenerative Fuel Cells. *J Electrochem Soc* **2022**, *169* (5), 054514. https://doi.org/10.1149/1945-7111/AC6C51.